ACS APPLIED NANO MATERIALS

www.acsanm.org Article

Interfacial Phase and Strain Modulation of CdSe on Reduced Graphene Oxide for Visible−Light Cr(VI) Photoreduction

Soumya Nandi,[#] Suvendu Ghosh,[#] Surajit Ghosh, and Tanusri Pal*

Cite This: https://doi.org/10.1021/acsanm.6c00578 Read Online

ACCESS | Metrics & More | Article Recommendations | Supporting Information

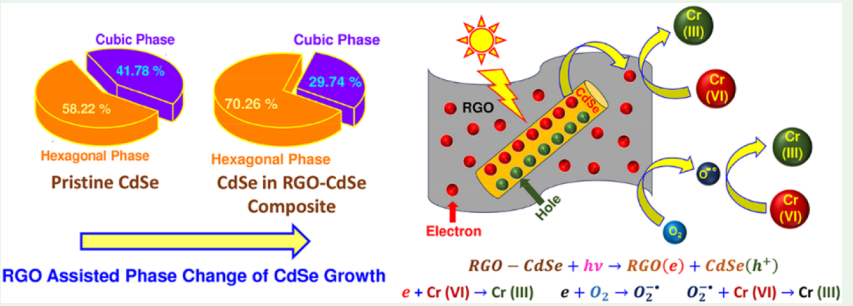

ABSTRACT: Hexavalent chromium [Cr(VI)] poses a serious environmental threat due to its high toxicity and mobility in aqueous systems. Here, we demonstrate that reduced graphene oxide (RGO) can act as an active interfacial substrate to modulate the crystal structure of cadmium selenide (CdSe), rather than serving solely as a conductive support. RGO−CdSe nanocomposites synthesized via an in situ hydrothermal route exhibit pronounced substrate-induced redistribution of hexagonal (wurtzite) and cubic (zinc-blende) phases, accompanied by systematic lattice strain modulation, as quantitatively revealed by powder X-ray diffraction and Rietveld refinement. These interfacial structural modifications enhance charge separation and transport, leading to markedly improved visible−light−driven photocatalytic reduction of Cr(VI). As a direct consequence of the RGO−induced phase redistribution and lattice strain modulation, the optimized RGO−CdSe composite delivers a 3.2-fold enhancement in Cr(VI) reduction efficiency relative to pristine CdSe. This structural-electronic synergy simultaneously accelerates reaction kinetics and increases the apparent quantum yield by factors of 4.6 and 2.96, respectively, while reducing the energy consumption by nearly 5.4-fold, thereby demonstrating the significant role of interfacial crystal engineering in boosting photocatalytic efficiency. The mechanism involves an interface-governed multielectron reduction pathway, where the RGO framework enables efficient electron extraction and accumulation. These interfacial structural changes correlate with improved charge separation and transport, resulting in enhanced visible−light−driven Cr(VI) reduction performance, highlighting the importance of interfacial phase and strain effects and offering a promising strategy for designing efficient photocatalysts for sustainable water remediation.

KEYWORDS: *RGO−CdSe composite, structural modulation, substrate-induced redistribution of phase, visible-light Cr(VI) reduction, interfacial charge transfer*

INTRODUCTION

The increasing release of toxic heavy metals into aquatic environments due to industrial activities poses serious risks to environmental sustainability and human health.[1,2] Among these contaminants, hexavalent chromium, Cr(VI), is particularly hazardous because of its high solubility, mobility, and strong carcinogenic nature.[3,4] Cr(VI) species readily migrate in water and accumulate in biological systems, causing severe health effects.[5−11] Conventional treatment methods, such as chemical precipitation,[12] adsorption,[13] and membrane separation[14] often suffer from high operational costs, limited efficiency at low concentrations, and secondary waste generation. Consequently, the development of energy-efficient and environmentally sustainable remediation strategies has become increasingly important.

Visible-light-driven photocatalytic reduction offers an attractive route for Cr(VI) remediation by converting highly toxic Cr(VI) into the much less harmful Cr(III) using solar energy.[15,16] The efficiency of this process strongly depends on the photocatalyst's ability to absorb visible light and to generate and separate charge carriers effectively. Cadmium selenide (CdSe) is a promising visible-light-active semiconductor due to its narrow bandgap and strong optical

Received: February 11, 2026
Revised: May 7, 2026
Accepted: May 13, 2026

absorption.[17,18] However, its photocatalytic performance is often limited by the rapid recombination of photogenerated charge carriers and inefficient interfacial charge extraction.[19,20]

To address these limitations, CdSe has been integrated with conductive carbon materials.[21] Reduced graphene oxide (RGO), with its large surface area and high electrical conductivity, is particularly attractive for facilitating charge transport and improving carrier separation.[22,23] Beyond acting as a conductive support, the two-dimensional framework of RGO can influence nucleation, crystal growth, and phase stability of semiconductor nanocrystals, thereby altering their internal structural organization.[24,25] Structural features such as phase distribution and lattice strain play critical roles in determining light absorption and charge-carrier dynamics in semiconductor photocatalysts.[26] Quantitative analysis using powder X-ray diffraction and Rietveld refinement, therefore, provides valuable insights into the relationship between the crystal structure and photocatalytic performance.

Although graphene-based semiconductor composites have been widely explored for photocatalytic applications, graphene derivatives are typically considered only as conductive supports that facilitate electron transport and suppress charge recombination. In CdSe−graphene systems, however, the influence of graphene on the crystallographic phase distribution and lattice strain of CdSe nanocrystals remains largely unexplored, despite their important roles in determining the band structure and charge-carrier dynamics.

In this work, RGO−CdSe nanocomposites were synthesized to investigate how interfacial interactions with reduced graphene oxide modify the structural properties of CdSe and influence photocatalytic activity. The composites exhibit significantly enhanced visible-light-driven Cr(VI) reduction compared with pristine CdSe, with faster kinetics, higher apparent quantum yield, and improved energy efficiency. By correlating structural parameters obtained from Rietveld refinement with photocatalytic performance, this study establishes a clear structure−property−function relationship in RGO−CdSe nanocomposites and highlights the active role of two-dimensional conductive substrates in tuning semiconductor crystal structure for environmental remediation.

EXPERIMENTAL SECTION

Chemicals

All materials utilized throughout this investigation were of analytical purity and used directly without further refinement. Compounds such as graphite powder, potassium persulfate ($K_2S_2O_8$), sodium nitrate ($NaNO_3$), phosphorus pentoxide (P_2O_5), cadmium nitrate tetrahydrate [$Cd(NO_3)_2{\cdot}4H_2O$], and sodium selenite (Na_2SeO_3) were procured from Sigma−Aldrich. Additional reagents, including concentrated sulfuric acid(H_2SO_4), potassium permanganate ($KMnO_4$), hydrochloric acid (HCl), ethylenediamine (ED; $C_2H_8N_2$), hydrogen peroxide (H_2O_2), were obtained from Merck.

Material Preparation

Preoxidized graphite was first exfoliated to obtain graphene oxide (GO).[27] RGO−CdSe composites were synthesized via a hydrothermal method. In a typical synthesis, GO was first dispersed in a mixed solvent of $C_2H_8N_2$ and double-distilled water (DD H_2O) under ultrasonication to obtain a homogeneous suspension. Subsequently, $Cd(NO_3)_2{\cdot}4H_2O$ and Na_2SeO_3 were added to the dispersion as Cd and Se precursors. The molar amounts of $Cd(NO_3)_2{\cdot}4H_2O$ and Na_2SeO_3 were kept constant at 2 mmol each, while the amount of GO was varied to obtain composites with different RGO contents. Specifically, 20, 30, 40, 50, and 60 mg of GO were used to prepare the 20RGO−CdSe, 30RGO−CdSe, 40RGO−CdSe, 50RGO−CdSe, and 60RGO−CdSe composites, respectively. The sample labels, therefore, correspond to the mass of GO (mg) introduced during synthesis while maintaining constant CdSe precursor concentrations. The resulting mixture was transferred to a Teflon-lined stainless-steel autoclave and heated at 170 °C for 12 h, enabling the in situ growth of CdSe nanostructures within the RGO framework under self-generated pressure. Following natural cooling to room temperature, the solid product was recovered by centrifugation, repeatedly washed with deionized water until near-neutral pH was attained, and subsequently vacuum−dried to yield a fine RGO−CdSe powder suitable for further characterization. For control studies, pristine CdSe was prepared through analogous procedures in the absence of GO. A schematic overview of the synthetic strategy is provided in Figure 1.

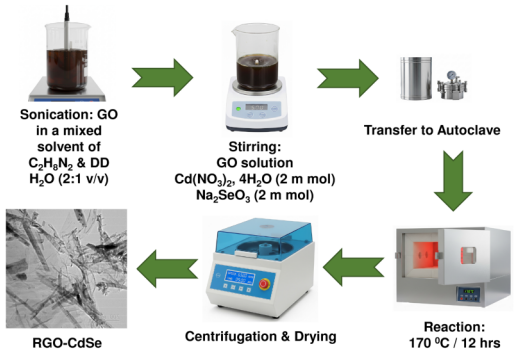

Figure 1. Schematic representation of the RGO−CdSe composite synthesis process.

Materials Characterization

Phase identification of both pure CdSe and the composite material was performed using powder X-ray diffraction (PXRD) with Cu K_α radiation, at room temperature, using a step size of 0.02°. The resulting patterns were refined by the Rietveld method using the FullProf software (Version 7.40). During refinement, the following parameters were varied until convergence was reached: background, scale factors, zero-point, unit cell parameters, atomic coordinates, and the profile coefficients of a Thomson−Cox−Hastings (T−C−H) Pseudo−Voigt axial divergence asymmetric function.

The structural and crystallographic details of the synthesized materials at the nanoscale were obtained from transmission electron microscopy (TEM) and high-resolution TEM (HRTEM) images, recorded on a JEOL JEM 2100F microscope operating at 200 kV. Raman spectra were recorded by using a LabRAM HR micro-Raman spectrometer from Horiba Scientific. The UV−visible absorption and photoluminescence (PL) characteristics were investigated using a spectrophotometer (Agilent Cary 5000 UV−vis-NIR) and a fluorescence spectrophotometer (Hitachi F-7000), respectively.

Evaluation of Photocatalytic Performance

The reduction efficiency of hexavalent chromium [Cr(VI)] under visible-light irradiation was systematically evaluated using the synthesized RGO−CdSe nanocomposite. Experiments were conducted in a custom-designed glass photoreactor equipped with a recirculating cold-water bath to maintain isothermal conditions. In each photocatalytic experiment, 20 mg of photocatalyst was dispersed in 40 mL of aqueous Cr(VI) solution prepared by dissolving 2.12 mg of $K_2Cr_2O_7$. This corresponds to an initial Cr(VI) concentration of approximately 18.8 mg L^{-1} (0.36 mM). The initial pH of the solution was ∼7 and was not externally adjusted during the photocatalytic reaction. At near-neutral pH, Cr(VI) primarily exists as $HCrO_4^-$/$Cr_2O_7^{2-}$ species in aqueous solution,[28,29] which are commonly involved in photocatalytic reduction processes. To ensure adsorption−desorption equilibrium between Cr(VI) species and the catalyst surface, the suspension was stirred for 30 min in the dark before initiating illumination. Control studies were also carried out to isolate individual contributions from (i) dark adsorption using the RGO−

https://doi.org/10.1021/acsanm.6c00578
ACS Appl. Nano Mater. XXXX, XXX, XXX−XXX

CdSe composite over a 100 min period and (ii) direct photocatalytic reduction of Cr(VI) in the absence of a catalyst under identical light exposure. The light intensity was calibrated using a Newport 843-R optical power meter. A 1000 W tungsten halogen lamp was used as the illumination source for photoreduction of Cr(VI). At 10 min intervals, 5 mL aliquots were withdrawn from the reaction suspension and centrifuged at 5000 rpm for 3 min to remove photocatalyst particles. The clear supernatant was then analyzed using a UV−vis spectrophotometer by monitoring the characteristic absorbance of Cr(VI) near ∼372 nm. The concentration at each time point (C) was obtained from the corresponding absorbance and normalized to the initial concentration (C_0). The reduction efficiency was therefore evaluated using the ratio C/C_0 to monitor the temporal evolution of Cr(VI) removal.

RESULTS AND DISCUSSION

The crystal structure, phase purity, and overall composition of the as-synthesized CdSe and RGO−CdSe composite were examined through XRD, with the corresponding diffraction spectra displayed as experimental data in Figure 2A and B. As

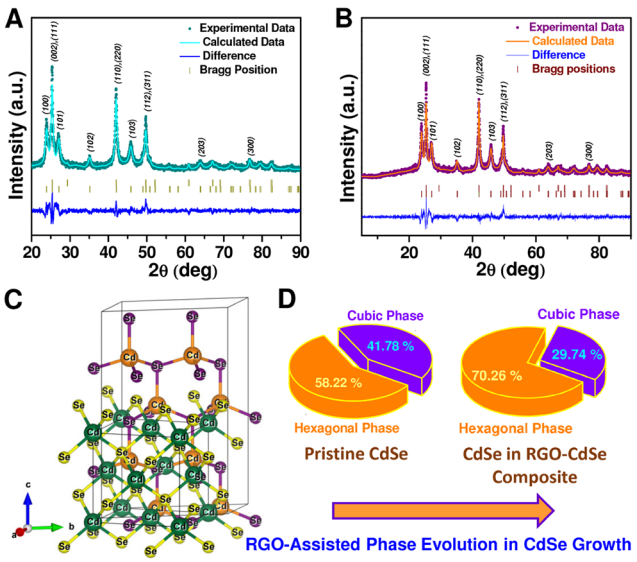

Figure 2. PXRD pattern with Rietveld refinement of XRD diffractograms using the Thompson−Cox−Hastings (TCH) Pseudo-Voigt axial divergence asymmetric function of (A) CdSe and (B) the RGO−CdSe composite. The observed experimental and calculated diffractograms, along with differences, are presented. (C) Phase diagram of the hexagonal and cubic phases of CdSe in the RGO−CdSe composite. (D) Hexagonal and cubic phase percentages of CdSe in pristine-CdSe and RGO−CdSe.

shown in the figure, the XRD profiles with reflections at 23.89°, 25.36°, 27.09°, 35.12°, 42.01°, 45.77°, 49.71°, 50.71°, and 52.07° nominally corresponding to the hexagonal wurtzite structure of CdSe (space group $P6_3mc$), as per JCPDS Card No. 08−0459[30] and can be indexed to the (100), (002), (101), (102), (110), (103), (112), (201), and (004) planes, respectively. All the indexed planes of CdSe are noticeably present in the CdSe nanocrystal grown on the RGO mat, i.e., in the RGO−CdSe composite. Collectively, these observations establish the coexistence of crystalline wurtzite CdSe and RGO within the composite. A close inspection, however, reveals slight deviations in the positions of several peaks. These discrepancies point to either lattice distortions induced by strain or minor inclusions of the cubic (zinc-blende) phase. The convolution of peaks in the 25.36°, 42.01°, and 49.71° regions further supports the possibility of a cubic phase contribution (JCPDS Card No. 19−0191),[31] but a definitive assignment awaits advanced structural analysis via Rietveld refinement.

To obtain quantitative structural parameters, the XRD data were subjected to Rietveld refinement using the FullProf program. Rietveld analysis for CdSe and RGO−CdSe, displayed in Figure 2A and B, respectively, along with the experimental data. The Rietveld refinement shows reasonable agreement between the calculated and experimental diffraction patterns. The relatively high R_p and R_{wp} values can be attributed to peak broadening associated with nanoscale crystallites, multiphase contributions, and possible preferred orientation effects, which are commonly observed in nanostructured materials. The values of the residual indices (R_{wp}, R_p, R_f, and χ^2) are listed in Table 1.

The crystal phase of these nanocrystals, typically the hexagonal wurtzite or the cubic zinc-blende structure, is a critical factor governing their electronic characteristics and stability. While the wurtzite phase is often reported as the thermodynamic product, controlling the synthesis to achieve a specific phase ratio remains a significant challenge. The Rietveld refinement analysis confirmed the existence of the cubic zinc-blende structure at 41.78%, alongside the wurtzite phase in pristine CdSe. A significant shift in the phase composition of CdSe is observed when nucleated on the RGO substrate. The fraction of the hexagonal (wurtzite) phase increases to 70.26%, compared to 58.22% in the free-standing nanocrystals, as obtained from the Rietveld refinement results (Table 1). This pronounced change strongly suggests that the RGO mat plays a dynamic role in directing crystal growth. The RGO mat provides a vast, two-dimensional (2D) surface with specific functional groups and defects. These sites can act as anchors for Cd^{2+} or Se^{2-} ions, creating a high density of nucleation centers. The hexagonal honeycomb lattice of RGO acts as an epitaxial template, lowering the nucleation energy barrier for the wurtzite phase through lattice matching and surface energy effects. Furthermore, the altered reaction kinetics and confinement provided by the 2D substrate likely contribute to the preferential stabilization of the hexagonal polymorph. This suggests the powerful utility of graphene-based substrates in exerting controlled synthesis over the crystal phase in semiconductor nanocomposites. The structural integrity of the CdSe nanocrystals synthesized on the RGO mat is confirmed by XRD analysis. A direct comparison of the patterns for pristine CdSe and the RGO−CdSe composite reveals that all characteristic diffraction peaks of the CdSe phases are distinctly preserved, with no emergence of extraneous impurity peaks, confirming the role of RGO as an inert solid support. For the hexagonal phase, a subtle contraction is observed in the c/a axial ratio, which decreases from 1.6334 in pristine CdSe to 1.6321 in the composite. The corresponding crystallite sizes and structural parameters were determined from the diffraction data, and these results are discussed in detail below.

Particle Size and Strain

The crystallite size of nanomaterials is commonly determined using the Debye−Scherrer formula, which relates peak broadening to size effects and intrinsic strain, and written as[32]

$$D = K\lambda / \beta_{hkl}\cos\theta \quad (1)$$

https://doi.org/10.1021/acsanm.6c00578
ACS Appl. Nano Mater. XXXX, XXX, XXX−XXX

Table 1. Rietveld Refinement Parameters of CdSe and RGO−CdSe Samples at Room Temperature Using the FullProf Program: Space Group, Phase Fraction, Cell Parameters, Cell Volume, and Discrepancy Factors[a]

Parameter	CdSe		RGO−CdSe	
	Hexagonal	Cubic	Hexagonal	Cubic
Space Group	$P6_3mc$	$F-43m$	$P6_3mc$	$F-43m$
Phase Fraction	58.22%	41.78%	70.26%	29.74%
Cell Parameters				
a (Å)	4.2972	6.0826	4.3012	6.0828
b (Å)	4.2972	6.0826	4.3012	6.0828
c (Å)	7.0188	6.0826	7.0202	6.0828
V (Å^3)	112.247	225.045	112.477	225.07
Discrepancy Factors				
R_p (%)	28.6		28.9	
R_{wp} (%)	27.8		27.5	
R_{exp} (%)	10.93		11.32	
χ^2	6.47		5.89	

Atomic Position

	Hexagonal		Cubic		Hexagonal		Cubic	
Phase	Cd	Se	Cd	Se	Cd	Se	Cd	Se
X	0.33333	0.33333	0.00000	0.25000	0.33333	0.33333	0.00000	0.25000
Y	0.66667	0.66667	0.00000	0.25000	0.66667	0.66667	0.00000	0.25000
Z	0.01384	0.39128	0.00000	0.25000	0.01063	0.38535	0.00000	0.25000

[a]R_p (%) and R_{wp} (%) are the profile residual and the weighted profile residual factors, respectively, used to verify the Rietveld refinement quality and the goodness of fit, chi-square (χ^2).

where, D is the average crystallite size, K, Debye−Scherrer constant (0.94), λ is the X-ray wavelength of CuK_α radiation (0.154 nm), β_{hkl} is the full width at half-maximum (FWHM) of the diffraction peak, and θ is the Bragg angle. To improve accuracy across multiple peaks, the modified Scherrer approach[33] was applied, and which is written as

$$\ln \beta_{hkl} = \ln\left(\frac{k\lambda}{D}\right) + \ln\left(\frac{1}{\cos\theta}\right) \quad (2)$$

A plot of ln β_{hkl} versus $\ln\left(\frac{1}{\cos\theta}\right)$ was done for all observable diffraction peaks, and the y-intercept gives the value of $\ln\left(\frac{k\lambda}{D}\right)$. Thus, the crystallite size (D) can be calculated from the expression

$$\frac{k\lambda}{D} = e^{\text{Intercept}} \quad (3)$$

Figure 3 displays the ln β versus ln (1/cosθ) plots for CdSe and RGO−CdSe. The resulting linear fits for CdSe where $y = -4.6451 - 1.58796x$ and $y = -4.31468 + 1.96155x$ for the cubic and hexagonal phases, respectively, and for RGO−CdSe, these are $y = -5.31581 + 1.32172x$ and $y = -4.3845 + 2.62363x$ for the cubic and hexagonal phases, respectively. Using the y-intercepts, the mean crystallite sizes were determined to be 10.37 and 14.43 nm for the hexagonal and cubic phases of CdSe, respectively, and for RGO−CdSe, these values are 11.12 and 28.22 nm.

The average crystallite size of the samples was estimated using the Williamson−Hall (W−H) method. In this approach, the broadening of XRD peaks arises from both finite crystallite size and lattice strain, along with possible structural imperfections. The analysis assumes a uniform distribution of strain in all crystallographic directions. Accordingly, the total peak broadening (β_{hkl}) is expressed as the sum of crystallite size broadening (β_s) and strain-induced broadening (β_ε),[34]

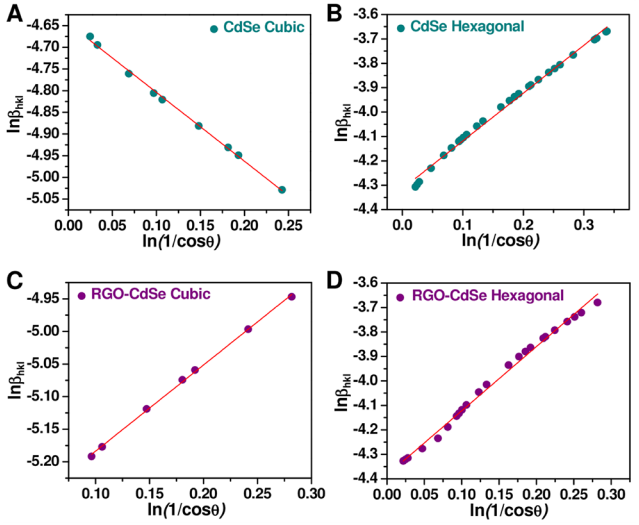

Figure 3. Plot of ln β_{hkl} versus ln (1/cosθ) obtained using the modified Scherrer equation for CdSe in the (A) cubic phase and (B) hexagonal phase, and for the RGO−CdSe composite in the (C) cubic phase and (D) hexagonal phase.

$$\beta_{hkl} = \beta_s + \beta_\varepsilon \quad (4)$$

This study employed by the W−H models with the help of Uniform Deformation Model (UDM). In UDM presumes isotropic strain in all crystallographic directions. Accordingly, the strain-induced broadening (β_ε) was determined using the following relation:[35]

$$\beta_\varepsilon = 4\varepsilon \times \tan\theta \quad (5)$$

The β_s in the above equation is given by Scherrer's expression as follows: $\beta_s = \frac{k\lambda}{D}\cos\theta$. Consequently, the overall

https://doi.org/10.1021/acsanm.6c00578
ACS Appl. Nano Mater. XXXX, XXX, XXX−XXX

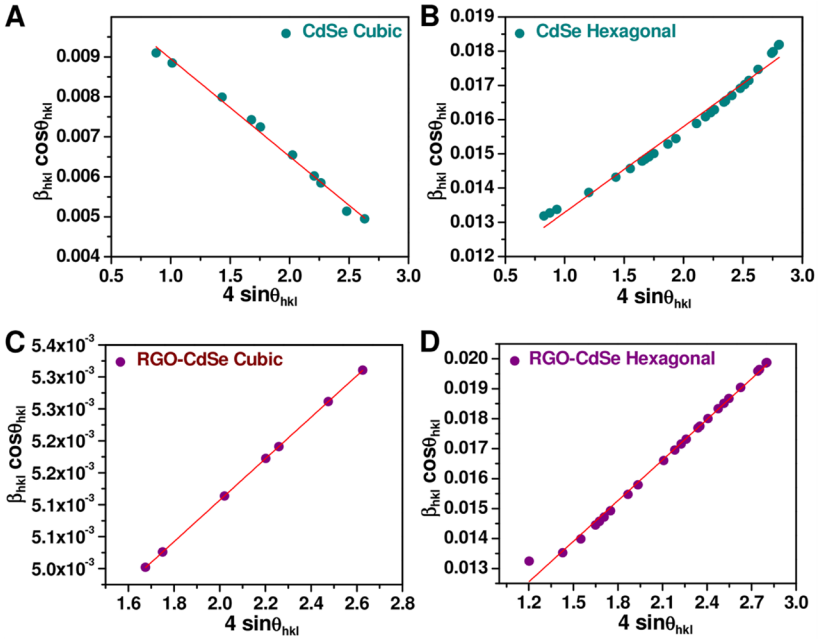

Figure 4. Crystallite strain analysis using Williamson-Hall plots: Plot of $\beta_{hkl}\cos\theta_{hkl}$ versus $4\sin\theta_{hkl}$ for CdSe in the (A) cubic phase and (B) hexagonal phase, and for the RGO−CdSe composite in the (C) cubic phase and (D) hexagonal phase assuming (UDM) analysis.

Table 2. Estimated Crystal Size and Crystalline Strain Using the Modified Scherrer Equation and the W−H Equation

	Crystallite Size (nm) from Mod. Scherrer Equation		Crystallite Size (nm) from W−H Plot		Strain (ε) x 10^{-3}	
	Cubic	Hexagonal	Cubic	Hexagonal	Cubic	Hexagonal
CdSe	14.43	10.37	12.16	12.86	−2.44	2.51
RGO−CdSe	28.22	11.12	30.74	19.45	0.325	4.52

peak broadening arising from both crystallite size and lattice strain can be expressed as[34]

$$\beta_{hkl} = \frac{k\lambda}{D\cos\theta_{hkl}} + 4\varepsilon\tan\theta_{hkl} \quad (6)$$

Where ε is the strain. Thus, size- and strain-induced broadening can be rewritten as follows:[36,37]

$$\beta_{hkl}\cos\theta_{hkl} = \frac{k\lambda}{D} + 4\varepsilon\sin\theta_{hkl} \quad (7)$$

By plotting $\beta_{hkl}\cos\theta_{hkl}$ against $4\sin\theta_{hkl}$ a linear fit is obtained. The crystalline size can be derived from the intercept, and the microstrain (ε) from the slope.

Figure 4 shows the W−H analysis of CdSe and RGO−CdSe for different phases, assuming (UDM) analysis. Calculations yielded sizes of ∼12.16 and 12.86 nm for the cubic and hexagonal phases, where a compressive strain (-2.44×10^{-3}) is observed for the cubic phase and tensile strain (2.51×10^{-3}) for the hexagonal phase of pristine CdSe. A significant increment in the crystallite size for the RGO−CdSe composite is observed, and the increased sizes are ∼30.74 nm for the cubic phase and 19.44 nm for the hexagonal phase. Interestingly, in the presence of the RGO matrix, the strain type of the CdSe cubic phase changes to tensile, which was compressive for the pristine CdSe. The calculated strain for the cubic and hexagonal phases of RGO−CdSe is 0.325×10^{-3} and 4.52×10^{-3}, respectively. The estimated crystal size and crystalline strain of CdSe and RGO−CdSe, using the Modified Scherrer equation and the W−H equation, is compared in Table 2.

Our results suggest a significant substrate-induced restructuring of phase-dependent strain states in the CdSe nanocrystals. While controlled synthesis of CdSe yielded a mixed-phase system (58.22% hexagonal, 41.78% cubic) with the cubic domains under compressive strain, growth on the basal plane of RGO reversed this signature: despite a higher hexagonal phase fraction (70.26%), the cubic phase exhibited tensile strain. This inversion indicates that RGO does not merely alter the phase ratio but fundamentally reengineers the internal architecture of the nanocrystal. Thus, the cubic phase transitions from a compressed inclusion within a hexagonal matrix to a tensile-strained foundational layer, highlighting the profound role of 2D substrates in dictating nanomaterial phase evolution and strain engineering.

The Williamson−Hall analysis was performed using the Uniform Deformation Model (UDM), which assumes isotropic microstrain. In nanostructured systems such as CdSe nanorods and RGO−CdSe composites, strain may include anisotropic contributions arising from directional growth and interfacial interactions. Accordingly, the extracted strain values represent effective average estimates, while the observed trends provide useful insights into strain modulation induced by RGO incorporation.

The microstructure of the RGO−CdSe composite was investigated by TEM and high-resolution TEM, as illustrated in Figure 5A. TEM images suggest that CdSe nanorods are uniformly anchored onto the corrugated, two-dimensional RGO framework, forming an interconnected hybrid structure

https://doi.org/10.1021/acsanm.6c00578
ACS Appl. Nano Mater. XXXX, XXX, XXX−XXX

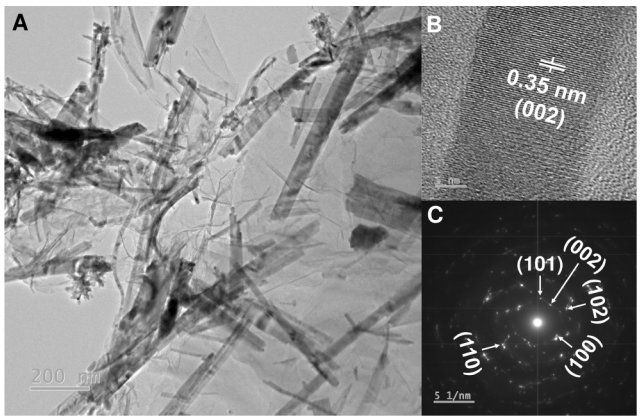

Figure 5. (A) TEM image of the RGO−CdSe composite. (B) HRTEM image and (C) SAED pattern acquired from CdSe nanorods in the RGO−CdSe composite.

with extensive interfacial contact. Such close coupling between the semiconductor nanorods and the conductive RGO scaffold is expected to facilitate efficient interfacial charge separation and electron transport. HRTEM analysis (Figure 5B) further confirms the crystalline nature of the CdSe nanorods, revealing well-resolved lattice fringes corresponding to the (002) crystallographic plane, consistent with the phase assignment obtained from X-ray diffraction. No evidence of a core−shell structure was detected; instead, localized contrast variations originate from overlapping or folded regions of multilayer RGO. The selected area electron diffraction (SAED) pattern (Figure 5C) shows sharp, well-defined diffraction spots displaying a clear reciprocal lattice pattern, which were observed and assigned to the (100), (002), (101), (102), and (110) planes of CdSe. The coexistence of multiple diffraction features suggests the presence of mixed crystalline domains, while the observation of both low and higher-index reflections indicates good overall crystallinity of the nanorods.

The structural properties and interface interactions of the RGO−CdSe composite were examined using Raman spectroscopy. The corresponding spectrum is presented in Figure 6A. Two dominant Raman signals appear near 1340 and 1592 cm^{-1}, representing the D and G bands of carbon-based materials. The D band is associated with disorder-induced breathing vibrations of A_{1g} symmetry at the K-point of the Brillouin zone. In contrast, the G band originates from the in-plane E_{2g} vibrational mode of sp^2-hybridized carbon atoms.[38] Besides the characteristic RGO features, several additional low-frequency peaks arise from the CdSe phase. The distinct mode observed at ∼206 cm^{-1} corresponds to the first-order longitudinal optical (1LO) phonon, while those at ∼287 and ∼405 cm^{-1} are associated with surface phonon modes and the second-order longitudinal optical (2LO) phonon, respectively.[38]

The D and G bands' intensity ratio (I_D/I_G) is frequently used to assess the extent of graphitic ordering.[39] For the RGO−CdSe system, an I_D/I_G ratio of ∼1.3 signifies effective GO reduction and corroborates the formation of well-developed RGO sheets within the composite.

The photocatalytic function of a semiconductor strongly depends on its visible light absorption capacity and its ability to maintain effective separation of photogenerated electrons and holes. To assess these aspects, optical absorption and PL measurements were carried out (Figure 6B and C). CdSe exhibits a clear absorption maximum near 620 nm, whereas an enhanced optical absorption throughout the visible range is observed for the RGO−CdSe composite. The Tauc plot analysis was employed to estimate the optical band gap (E_g) of CdSe as, $\alpha h\nu = A(h\nu - E_g)^n$, with $n = 1/2$ for direct transitions and $n = 2$ for indirect transitions.[40] The variation of $(\alpha h\nu)^2$ with photon energy,[41] presented in the inset of Figure 6B, gives an estimated bandgap energy (E_g) of ∼2.00 eV. This value is blue-shifted relative to bulk CdSe ($E_g \approx 1.74$ eV),[42,43] which is consistent with the expected quantum confinement effect.

Figure 6C presents the PL spectrum of the as-synthesized pristine CdSe nanorods. Under excitation at 610 nm, a well-defined emission band appears at 723 nm. The emission appearing at a lower energy than the optical band gap signifies a noticeable Stokes shift, arising from carrier relaxation to energetically lower states and from recombination through surface-related defect traps. Thus, the PL features arise from the effects of both intrinsic and defect-mediated emission processes. Conversely, a marked quenching of PL intensity was observed for the RGO−CdSe composite, highlighting strong electronic coupling between the RGO sheets and CdSe. The quenching behavior indicates efficient charge extraction, as photogenerated electrons in CdSe readily migrate to the highly conductive RGO network, thereby suppressing electron−hole recombination. A similar PL quenching behavior has been reported in other RGO−CdSe composite systems.[21,44] The remaining holes in the CdSe valence band actively participate in oxidation reactions, thereby enhancing photocatalytic activity.

The reduced photoluminescence intensity observed for the RGO−CdSe composite suggests more efficient separation of photogenerated electron−hole pairs, which can be attributed to interfacial charge transfer between CdSe nanorods and the conductive RGO framework. Such interfacial coupling

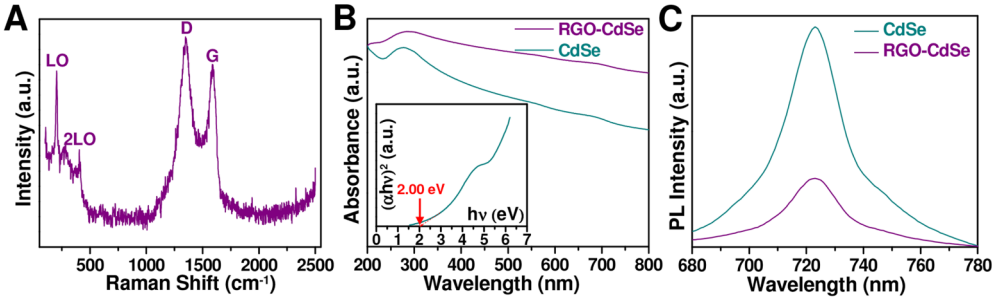

Figure 6. (A) Raman profiles of RGO−CdSe composite. (B) Optical absorption curves with an inset depicting the Tauc plot $(\alpha h\nu)^2$ vs photon energy for CdSe, and (C) photoluminescence response.

https://doi.org/10.1021/acsanm.6c00578
ACS Appl. Nano Mater. XXXX, XXX, XXX−XXX

facilitates the migration of photogenerated electrons from CdSe to the RGO network, thereby suppressing recombination. While the structural analyses indicate variations in phase composition and lattice strain, the present optical results primarily support improved charge separation and interfacial electron transport as key contributors to the enhanced photocatalytic performance.

Photocatalytic Reduction of Cr(VI) under Visible Light Using RGO−CdSe Composite

Prior to evaluating the photocatalytic reduction of Cr(VI), control experiments were conducted to examine its stability under visible light in the absence of a catalyst, as well as in the presence of the RGO−CdSe composite without illumination. The UV−vis absorption spectra obtained under these conditions confirmed that the concentration of Cr(VI) remained essentially unchanged when no photocatalyst was present [Figure S1A in the Supporting Information (SI)], indicating that visible light alone cannot drive the reduction process. Moreover, only a slight decrease in Cr(VI) concentration was detected within 30 min when the RGO−CdSe composite was stirred in the dark (Figure S1B), suggesting minimal adsorption capacity. These results clearly suggest that both the photocatalyst and visible light irradiation are indispensable for initiating Cr(VI) reduction.

The photocatalytic reduction of Cr(VI) by pristine CdSe and the RGO−CdSe composites was systematically investigated under visible light irradiation (Figure S2A-F, SI). In all cases, the characteristic absorption bands of Cr(VI) progressively decreased with increasing irradiation time. A direct comparison of normalized absorption intensities under identical conditions (Figure S3A, SI) revealed that the RGO−CdSe composite exhibited significantly superior activity relative to CdSe alone. This enhancement is attributed to the heterostructured interface between RGO and CdSe, where favorable band alignment facilitates efficient charge separation and accelerates electron transfer, thereby boosting the photocatalytic Cr(VI) reduction process.

The photocatalytic reduction of Cr(VI) was quantitatively assessed using the relation:[45]

$$\text{Reduction efficiency}\ (\%) = \left(1 - \frac{C}{C_0}\right) \times 100\% \tag{8}$$

where C_0 and C represent the initial and instantaneous concentrations of Cr (VI) at time $t = 0$ and at irradiation time t, respectively. The comparative results are shown in Figure 7A. After 120 min of visible-light exposure, CdSe achieved only 23% Cr(VI) reduction efficiency, reflecting its limited activity. In contrast, the RGO−CdSe composite reached 74% efficiency under identical conditions. This remarkable improvement stems from RGO's role as a conductive matrix, which accelerates electron transport and suppresses charge recombination.

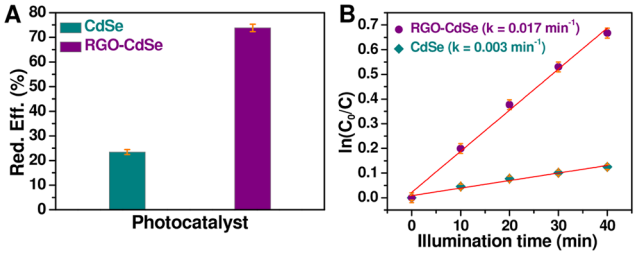

Figure 7. Visible-light-driven photocatalytic activity: (A) temporal evolution of Cr(VI) reduction efficiency and (B) corresponding pseudo-first-order kinetic plots $\ln\left(\frac{C_0}{C}\right)$ vs time for CdSe and the RGO−CdSe composite.

Additionally, the intimate contact between RGO nanosheets and CdSe nanoparticles promotes interfacial charge separation, further speeding up the reduction of Cr(VI). These cooperative effects emphasize the crucial role of RGO in enhancing the overall photocatalytic performance of the composites.

To elucidate the photocatalytic Cr(VI) reduction pathway, kinetic studies were performed within the Langmuir−Hinshelwood (L-H) framework, a widely applied model for heterogeneous photocatalysis, particularly when adsorption−desorption equilibria influence the overall rate.[46] According to this model, the reaction rate (r, $\text{mgL}^{-1}\text{min}^{-1}$) is expressed as[47]

$$r = -\frac{dC}{dt} = \frac{k_r K C}{1 + KC} \tag{9}$$

where C denotes the pollutant concentration (mgL^{-1}), k_r is the intrinsic rate constant ($\text{mgL}^{-1}\text{min}^{-1}$), the adsorption equilibrium constant (Lmg^{-1}) is denoted by K. This formulation assumes rapid adsorption−desorption equilibrium, with the reaction occurring at adsorbed sites. Under dilute concentration conditions where $KC \ll 1$, the above expression simplifies to

$$r \approx -k_r K C = kC \tag{10}$$

where $k = k_r K$ represents the apparent pseudo-first-order rate constant. Integration of this expression gives the well-known pseudo-first-order kinetic equation:[48]

$$\ln\left(\frac{C_0}{C}\right) = kt \tag{11}$$

The photocatalytic reduction kinetics were analyzed using a pseudo-first-order model, which is generally applicable for dilute pollutant concentrations commonly employed in photocatalytic studies. As shown in Figure 7B, the linear correlation between $\ln(C_0/C)$ and irradiation time enabled determination of the rate constants. The RGO−CdSe composite showed k = 0.017 min^{-1}, nearly 5.6-fold higher than that of CdSe (0.003 min^{-1}). This enhancement is attributed to the electron-accepting and transport properties of the RGO framework, which suppresses charge recombination.

The apparent quantum yield (AQY) provides a quantitative measure of how effectively incident photons are converted into chemical output, thereby reflecting the light-to-chemical conversion efficiency of a photocatalyst. It is defined as[49]

$$\text{AQY}(\%) = \frac{\text{Number of Cr(VI) ions reduced}}{\text{Number of incident photon}} \times 100 \tag{12}$$

In practical applications, this can be further expanded to

$$\text{AQY}(\%) = \frac{N_{\text{Reduced}}}{P_{\text{Incident}} \times t_{\text{Exposure}}/E_{\text{Photon}}} \times 100 \tag{13}$$

In this work, the AQY was calculated on the basis of the number of Cr(VI) ions reduced per incident photon, following a molecule-based definition commonly used in photocatalytic reduction studies. Since the reduction of Cr(VI) to Cr(III) involves multiple electron-transfer steps, the reported AQY

https://doi.org/10.1021/acsanm.6c00578
ACS Appl. Nano Mater. XXXX, XXX, XXX−XXX

represents an apparent value that provides a comparative measure of photocatalytic efficiency under identical illumination conditions.

Here, $N_{Reduced}$ is the number of Cr(VI) ions reduced, calculated from the initial concentration and reduction fraction; $P_{Incident}$ is the incident light power (W); $t_{Exposure}$ is the irradiation duration (in s); and E_{Photon} is the energy of an individual photon. The photon flux used in the AQY calculation was estimated based on the measured light intensity of the tungsten−halogen lamp under the experimental conditions. The detailed calculation of AQY is presented in SI. The AQY of the RGO−CdSe composite (~0.16%) is approximately three times higher than that of pristine CdSe (~0.054%), confirming the role of RGO in promoting charge separation and electron transport. The reported AQY values are based on the number of reduced Cr(VI) species without accounting for the electron stoichiometry; since the reduction of Cr(VI) to Cr(III) involves a three-electron transfer per Cr ion, the actual AQY values would be three times higher when expressed on an electron basis.

Since photocatalytic applications are closely tied to energy demand, the "electrical energy per order" (EE/O) was also evaluated, representing the electrical energy (kWh) required to reduce pollutant concentration by 1 order of magnitude in 1 m^3 of solution, thus serving as a key metric for assessing process energy economy:[50]

$$EE/O = \frac{\text{lamp power (W)} \times \text{time(h)} \times 1000}{\text{treated volume } (V) \times \log(C_0/C)} \quad (14)$$

where V is the treated solution volume (L). In the present study, a 1 kW tungsten−halogen lamp was used as the irradiation source. Lower EE/O values indicate higher energy efficiency of the photocatalytic process. As derived from log (C_0/C) vs irradiation dose plots [Figure S3B, in SI], the *EE/O* values were 314 and 57.6 kWh m^{-3} $order^{-1}$ for CdSe and RGO−CdSe, respectively. This nearly 5.45-fold reduction suggests substantial energy savings upon RGO incorporation, demonstrating the enhanced energy efficiency of the composite.

Extending these analyses, the photocatalytic efficiency of CdSe undergoes substantial enhancement once RGO is incorporated, leading to the formation of RGO−CdSe composite. The role of RGO concentration within the RGO−CdSe system was systematically investigated under uniform conditions. Notably, photocatalytic activity steadily improves with increasing RGO fraction, achieving maximum performance at 40RGO−CdSe (denoted as RGO−CdSe in this paper), but declines when the RGO content is further increased (Figure 8A). To quantify this, the apparent rate constant (k) was determined for each sample, and its dependence on RGO concentration is shown in Figure 8B. All composites exhibit significantly higher k values compared to pristine CdSe, confirming the cooperative interaction between RGO and CdSe. Consistent with the photocatalytic reduction trend, the maximum rate constant was obtained for 40RGO−CdSe. Similarly, the AQY of the composites follows the same trend (Figure 8C), reaching its peak for 40RGO−CdSe, whereas the EE/O displays the opposite behavior (Figure 8D), attaining its lowest value at 40RGO−CdSe. The observed variations can be rationalized as follows: at low RGO concentrations, the amount of RGO is inadequate to provide sufficient interfacial area for CdSe dispersion, while excessive

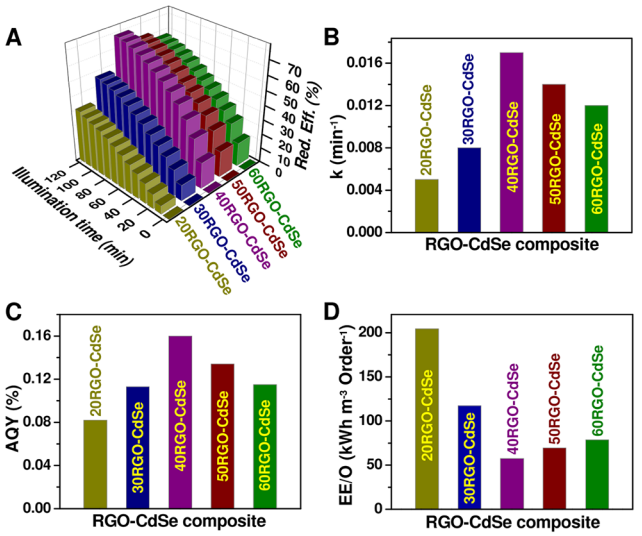

Figure 8. Influence of RGO content on photocatalytic behavior: (A) variation in Red. Eff., (B) corresponding k, (C) AQY, and (D) EE/O for the evaluated samples.

RGO tends to shield CdSe nanorods, thereby suppressing exciton generation and charge transfer.

Upon visible-light irradiation, CdSe nanorods generate electron−hole pairs. Owing to the intimate interfacial contact and favorable band alignment, photogenerated electrons are efficiently transferred from the conduction band of CdSe to the RGO framework. The RGO network acts as a conductive electron reservoir, suppressing charge recombination and enabling electron accumulation at the CdSe/RGO interface. These accumulated electrons directly participate in the multielectron reduction of aqueous Cr(VI) species to Cr(III).[51,52] In parallel, dissolved O_2 can be reduced to superoxide radicals ($O_2^{-\bullet}$), which may also contribute to Cr(VI) conversion through indirect reduction pathways.[51,52] Meanwhile, photogenerated holes remaining in the valence band of CdSe are consumed through water oxidation or other surface oxidation reactions, thereby maintaining charge neutrality within the system.

The pronounced quenching of photoluminescence observed for the RGO−CdSe composite suggests efficient interfacial charge separation and electron extraction, which contributes to the enhanced photocatalytic Cr(VI) reduction activity. The proposed photocatalytic pathway is inferred from the observed photoluminescence quenching and established literature reports on semiconductor−carbon hybrid systems,[53,54] and therefore represents a plausible mechanistic hypothesis rather than direct experimental confirmation. A comparison of the photocatalytic performance of the RGO−CdSe composite with previously reported photocatalysts for Cr(VI) reduction is provided in Table S1 (Supporting Information), demonstrating its competitive performance under visible-light irradiation.

The influence of the solution pH on the photocatalytic reduction of Cr(VI) was investigated. The reduction efficiency was higher under acidic conditions and gradually decreased with increasing pH (Figure S4, in SI). This behavior can be attributed to the favorable adsorption of protonated Cr(VI) species and enhanced electron transfer at a lower pH. Under alkaline conditions, electrostatic repulsion between chromate ions and the catalyst surface reduces the reduction efficiency.

https://doi.org/10.1021/acsanm.6c00578
ACS Appl. Nano Mater. XXXX, XXX, XXX−XXX

The operational stability of the RGO−CdSe photocatalyst was further evaluated through recycling experiments under identical reaction conditions. As shown in Figure S5A, the photocatalytic reduction efficiency of Cr(VI) decreased only slightly after five successive cycles, retaining more than ∼88% of its initial activity, indicating good reusability of the catalyst. To examine structural stability, XRD analysis of the catalyst recovered after five photocatalytic cycles was performed (Figure S5B). The diffraction pattern remained essentially unchanged compared with the fresh sample, confirming that the crystalline structure of the RGO−CdSe composite was preserved during the photocatalytic process. These results suggest that the composite possesses good structural stability under the present reaction conditions.

Collectively, the enhanced Cr(VI) reduction activity of the RGO−CdSe nanocomposites can be attributed to RGO-induced interfacial electronic interactions that promote efficient charge separation and electron transport. This interfacial coupling facilitates multielectron transfer to Cr(VI), resulting in superior visible-light photocatalytic performance compared with pristine CdSe. A schematic illustration of the proposed photocatalytic Cr(VI) reduction mechanism over the RGO−CdSe composite is presented in Figure 9.

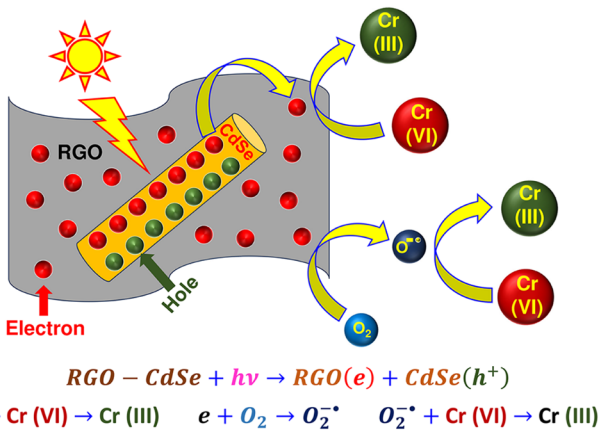

Figure 9. Mechanistic of photocatalytic chromium reduction by the RGO−CdSe composite.

CONCLUSION

In summary, we have demonstrated that RGO plays an important role in modulating the crystal structure and photocatalytic behavior of CdSe nanorods. Quantitative analysis via Rietveld refinement of XRD data reveals a substrate-induced redistribution of hexagonal wurtzite and cubic zinc-blende phases, along with lattice strain variation, which may contribute to charge-carrier separation and transport. As a result, the optimized RGO−CdSe nanocomposite exhibits significantly enhanced visible-light-driven Cr(VI) reduction efficiency, accelerated reaction kinetics, higher quantum efficiency, and reduced energy consumption compared to pristine CdSe. The photocatalytic reduction was also found to be pH-dependent, showing higher efficiency under acidic conditions due to favorable adsorption and electron transfer processes. Performance is consistent with that efficient interfacial electron extraction by the RGO framework, which enables direct multielectron reduction of Cr(VI) to Cr(III), while photogenerated holes are consumed via oxidation pathways to maintain charge neutrality. These observations suggest that the enhanced photocatalytic performance may be associated with interfacial phase and strain effects introduced by RGO incorporation. In addition, the RGO−CdSe composite exhibits good stability and reusability over repeated photocatalytic cycles, indicating its potential for practical applications. These results indicate that the incorporation of RGO influences the structural characteristics of CdSe and is accompanied by improved photocatalytic performance, providing useful guidance for the design of semiconductor−carbon heterostructures for sustainable water remediation. These findings also highlight a viable route for fine-tuning material properties through substrate-mediated phase and strain engineering in nanocomposite systems.

ASSOCIATED CONTENT

Supporting Information

The Supporting Information is available free of charge at https://pubs.acs.org/doi/10.1021/acsanm.6c00578.

UV−vis absorption spectrum of Cr(VI) aqueous solution without a catalyst under light illumination and with RGO−CdSe catalyst under dark, temporal evolution of UV−vis absorption spectra of Cr(VI) under illumination in the presence of CdSe, and RGO−CdSe composite with varying RGO content in the composite, time-dependent variation of normalized Cr(VI) concentration (C/C_0) in the presence of CdSe and RGO−CdSe composites with different RGO loadings, and dependence of $\log(C_0/C)$ on illumination dose for RGO−CdSe composites containing varying amounts of RGO, calculation of Apparent Quantum Yield (AQY) for the RGO−CdSe composite, variation of Cr(VI) reduction efficiency of the RGO−CdSe composite at different pH values, comparison of photocatalytic Cr(VI) reduction performance of RGO−CdSe with reported photocatalysts under visible-light irradiation, reduction efficiency of RGO−CdSe composite for five consecutive degradation cycles, XRD pattern of the RGO−CdSe composite after five cycles of Cr(VI) degradation in an aqueous medium (PDF)

AUTHOR INFORMATION

Corresponding Author

Tanusri Pal − *Department of Physics, Midnapore College (Autonomous), Midnapore 721101, India;* orcid.org/0000-0003-2623-5812; Email: tanusripal@midnaporecollege.ac.in

Authors

Soumya Nandi − *Department of Physics, Midnapore College (Autonomous), Midnapore 721101, India*

Suvendu Ghosh − *Optoelectronic Materials Lab, Department of Physics, Vidyasagar University, Midnapore 721102, India*

Surajit Ghosh − *Optoelectronic Materials Lab, Department of Physics, Vidyasagar University, Midnapore 721102, India;* orcid.org/0000-0001-6604-8857

Complete contact information is available at: https://pubs.acs.org/10.1021/acsanm.6c00578

Author Contributions

#S.N. and S.G. contributed equally to this work.

https://doi.org/10.1021/acsanm.6c00578
ACS Appl. Nano Mater. XXXX, XXX, XXX−XXX

Notes

The authors declare no competing financial interest.

■ ACKNOWLEDGMENTS

The work is carried out with the financial support of the Department of Science and Technology and Biotechnology (DSTBT), Government of West Bengal, India, under Grant No. 625(Sanc)/STBT-11012(26)/2/2024-ST SEC. The authors also thank the Department of Science and Technology (DST) and the University Grants Commission (UGC), New Delhi, India, for infrastructural support extended to the Department of Physics, Vidyasagar University, through the FIST and SAP schemes. In addition, the authors are grateful to the University Science Instrumentation Centre (USIC), Vidyasagar University, for assistance with photoluminescence measurements.

■ REFERENCES

(1) Zou, Y.; Wang, X.; Khan, A.; Wang, P.; Liu, Y.; Alsaedi, A.; Hayat, T.; Wang, X. Environmental Remediation and Application of Nanoscale Zero-Valent Iron and Its Composites for the Removal of Heavy Metal Ions: A Review. *Environ. Sci. Technol.* **2016**, *50*, 7290−7304.

(2) Saravanan, P.; Saravanan, V.; Rajeshkannan, R.; Arnica, G.; Rajasimman, M.; Baskar, G.; Pugazhendhi, A. Comprehensive Review on Toxic Heavy Metals in the Aquatic System: Sources, Identification, Treatment Strategies, and Health Risk Assessment. *Environ. Res.* **2024**, *258*, 119440.

(3) He, J.; Liu, L.; Fu, N.; Zhao, Y.; Zhang, L.; Feng, L.; Teng, G.; Li, X.; Zhang, C. Construction of Sulfur-Vacancy-Modified 0D/2D S-Scheme Heterojunction for Enhancing Photocatalytic Cr(VI) Reduction. *ACS Mater. Lett.* **2025**, *7*, 566−575.

(4) Wu, E.; Zhou, J.; Ren, D.; He, H.; Pan, J.; Tang, C.; Zhuang, X. Structural-Interfacial Engineering of MOF-Functionalized Aerogels for Efficient Photocatalytic Reduction of Cr(VI). *J. Hazard. Mater.* **2025**, *495*, 139019.

(5) Dong, W.; Liu, C.; Lin, G.-B.; Zhang, Y.-C.; Li, H.-B.; Juhasz, A. L.; Liu, C.; Ma, L. Q. Chromium Oral Bioavailability in 16 Contaminated Soils from Different Sources: Mouse Model Development and Cr Speciation in Soil and Mouse Tissues. *Environ. Sci. Technol.* **2025**, *59* (9), 4318−4329.

(6) Sekaran, M.; Thiagarajan, K. Biochemical Detoxification of Hexavalent Chromium (Cr^{6+}) by the Endophytic Fungus Aspergillus Ruber Isolated from the Marine Alga Portieria Hornemannii. *J. Environ. Chem. Eng.* **2025**, *13*, 117254.

(7) Xin, X.; Tian, X.; Yu, H.; Han, Z. Synthesis of Hybrid Phosphomolybdates and Application as Highly Stable and Effective Catalyst for the Reduction of Cr(VI). *Inorg. Chem.* **2018**, *57*, 11474−11481.

(8) Hou, L.; Zhang, Y.; Ma, Y.; Wang, Y.; Hu, Z.; Gao, Y.; Han, Z. Reduced Phosphomolybdate Hybrids as Efficient Visible-Light Photocatalysts for Cr(VI) Reduction. *Inorg. Chem.* **2019**, *58*, 16667−16675.

(9) An, W.; Zhang, X.; Niu, J.; Ma, Y.; Han, Z. Unusual Hexa-Nuclear Cadmium Cluster Functionalized Phosphomolybdate as Effective Photoelectrochemical Sensor for Trace Cr (VI) Detection. *Chin. Chem. Lett.* **2022**, *33* (9), 4400−4404.

(10) Song, H.; Guo, M.-S.; Wang, J.-F.; Liu, Y.-Q.; Bi, H.-X.; Du, J.; An, W.-T.; Ma, Y.-Y.; Han, Z.-G. Reduced Phosphomolybdate as Photoassisted Electrochemical Crystalline Sensor for Trace Cr(VI) Detection. *Polyoxometalates* **2024**, *3*, 9140065.

(11) He, J.-Y.; Bi, H.-X.; Liu, Y.-Q.; Guo, M.-S.; An, W.-T.; Ma, Y.-Y.; Han, Z.-G. Bridging Component Strategy in Phosphomolybdate-Based Sensorsfor Electrochemical Determination of Trace Cr(VI). *Inorg. Chem.* **2024**, *63*, 842−851.

(12) Femina Carolin, C.; Kamalesh, T.; Kumar, P. S.; Rangasamy, G. A Critical Review on the Sustainable Approaches for the Removal of Toxic Heavy Metals from Water Systems. *Ind. Eng. Chem. Res.* **2023**, *62*, 8575−8601.

(13) Shakiba, M.; Abdouss, M.; Mazinani, S.; Kalaee, M.; Neisiany, R. E. Development of a High-Performance Core/Double-Layered Sheath Nanofibrous Membrane for Continuous Cr(VI) Removal in Adsorption-Filtration Systems. *J. Environ. Chem. Eng.* **2025**, *13*, 115728.

(14) Kanani-Jazi, M. H.; Akbari, S. Quantitative XPS Analysis of Amine-Terminated Dendritic Functionalized Halloysite Nanotubes Decorated on PAN Nanofibrous Membrane and Adsorption/Filtration of Cr(VI). *Chem. Eng. J.* **2024**, *482*, 148746.

(15) Yang, K.; Wei, W.; Xie, X.; Zhang, H.; Li, H.; Wang, P.; Wang, K.; Dai, S.; Liu, Y.; Zheng, W.; et al. Harnessing Solar Energy for the Photocatalytic Reduction of Hexavalent Chromium: A High-Performance Yarrowia lipolytica −CdS Biohybrid System. *ACS Appl. Mater. Interfaces* **2025**, *17* (19), 28327−28335.

(16) Han, X.; Chen, L.; Liu, R.; Li, X.; Yan, H.; Kong, X.; Zhou, H.; Li, X.; Wang, S.; Li, Y.; Zhu, H.; Zhong, D.; Hao, H. Nanoengineering *Z*-Scheme Heterostructures in CdS Quantum Dot-Decorated Holmium-Based Metal−Organic Frameworks: Photothermal Catalytic Reduction of Hexavalent Chromium in Contaminated Waters. *ACS Appl. Nano Mater.* **2025**, *8*, 12189−12201.

(17) Chen, S.; Petersen, N.; Valsson, O.; Girard, M.; Wang, H. I. Understanding and Controlling the Colloidal Stability of CdSe Nanoplatelets by Solvation Force Engineering. *J. Am. Chem. Soc.* **2025**, *147*, 35347−35354.

(18) Shen, X.; Guyot-Sionnest, P. Midinfrared Electroluminescence from CdSe Quantum Dots. *ACS Nano* **2025**, *19*, 5811−5817.

(19) Costi, R.; Saunders, A. E.; Elmalem, E.; Salant, A.; Banin, U. Visible Light-Induced Charge Retention and Photocatalysis with Hybrid CdSe-Au Nanodumbbells. *Nano Lett.* **2008**, *8*, 637−641.

(20) Haldar, K. K.; Sinha, G.; Lahtinen, J.; Patra, A. Hybrid Colloidal Au-CdSe Pentapod Heterostructures Synthesis and Their Photocatalytic Properties. *ACS Appl. Mater. Interfaces* **2012**, *4* (11), 6266−6272.

(21) Lin, Y.; Zhang, K.; Chen, W.; Liu, Y.; Geng, Z.; Zeng, J.; Pan, N.; Yan, L.; Wang, X.; Hou, J. G. Dramatically Enhanced Photoresponse of Reduced Graphene Oxide with Linker-Free Anchored CdSe Nanoparticles. *ACS Nano* **2010**, *4*, 3033−3038.

(22) Xie, G.; Zhang, K.; Guo, B.; Liu, Q.; Fang, L.; Gong, J. R. Graphene-Based Materials for Hydrogen Generation from Light-Driven Water Splitting. *Adv. Mater.* **2013**, *25*, 3820−3839.

(23) Mkhalid, I. A.; Shawky, A. Visible Light-Active CdSe/rGO Heterojunction Photocatalyst for Improved Oxidative Desulfurization of Thiophene. *Ceram. Int.* **2020**, *46*, 20769−20776.

(24) Cheng, G.; Akhtar, M. S.; Yang, O. B.; Stadler, F. J. Novel Preparation of Anatase TiO2@reduced Graphene Oxide Hybrids for High-Performance Dye-Sensitized Solar Cells. *ACS Appl. Mater. Interfaces* **2013**, *5* (14), 6635−6642.

(25) Wang, H.; Robinson, J. T.; Diankov, G.; Dai, H. Nanocrystal Growth on Graphene with Various Degrees of Oxidation. *J. Am. Chem. Soc.* **2010**, *132*, 3270−3271.

(26) Luo, J.; Zhang, S.; Sun, M.; Yang, L.; Luo, S.; Crittenden, J. C. A Critical Review on Energy Conversion and Environmental Remediation of Photocatalysts with Remodeling Crystal Lattice, Surface, and Interface. *ACS Nano* **2019**, *13* (9), 9811−9840.

(27) Chakraborty, K.; Das, P.; Chakrabarty, S.; Pal, T.; Ghosh, S. AC Conduction and Time − Temperature Superposition Scaling in a Reduced Graphene Oxide − Zinc Sulfide Nanocomposite. *ChemPhysChem* **2016**, *17*, 1518−1523.

(28) Dvoynenko, O.; Lo, S.-L.; Chen, Y.-J.; Chen, G. W.; Tsai, H.-M.; Wang, Y.-L.; Wang, J.-K. Speciation Analysis of Cr (VI) and Cr (III) in Water with Surface-Enhanced Raman Spectroscopy. *ACS Omega* **2021**, *6* (3), 2052−2059.

(29) Szabó, M.; Kalmár, J.; Ditrói, T.; Bellér, G.; Lente, G.; Simic, N.; Fábián, I. Equilibria and Kinetics of Chromium (VI) Speciation in Aqueous Solution − A Comprehensive Study from pH 2 to 11, *Inorg. Chim. Acta* **2018**, *472*, 295−301.

https://doi.org/10.1021/acsanm.6c00578
ACS Appl. Nano Mater. XXXX, XXX, XXX−XXX

(30) Ran, W.; Ding, Q.; Wang, Z.; Shen, G. Bioinspired Dual-Mode Nanowire Photodetector with High Responsivity for Wide Dynamic Range Image Sensing. *Adv. Funct. Mater.* **2026**, *36*, No. e24536.
(31) Dayal, S.; Kopidakis, N.; Olson, D. C.; Ginley, D. S.; Rumbles, G. Direct Synthesis of CdSe Nanoparticles in Poly(3-hexylthiophene). *J. Am. Chem. Soc.* **2009**, *131*, 17726−17727.
(32) Wei, F.; Wang, J.; Wang, T.; Gao, S.; Liu, X.; Wang, J.; Li, J.; Song, W.; Fan, X. Efficient Rigid and Flexible Perovskite Solar Cells with Uniform Crystallization and Weak Lattice Vibration via Interface Defect Passivation. *Nano Lett.* **2025**, *25*, 15249−15255.
(33) Ashiq, M. G. B. Dielectric, Impedance and Electric Modulus Properties of Lanthanum-Doped Zinc Spinel Ferrite ($ZnLa_xFe_{2-x}O_4$) Nanomaterials. *Ceram. Int.* **2025**, *51*, 52989−53003.
(34) Bisht, P.; Meenakshi; Gaur, A.; Mahato, R. N. Structural and Magnetocaloric Properties $(0.75)La_{0.7}Ca_{0.3}MnO_3/(0.25)$-$La_{0.84}Sr_{0.16}MnO_3$ Nanocomposite. *Phys. B* **2021**, *619*, 413215.
(35) Mesrar, M.; Mesrar, L.; Elbasset, A.; Echatoui, N.-S.; Abdi, F.; Lamcharfi, T.-D. Study on the Structure, Morphology, Dielectric, and Piezoelectric Properties of Large-Grain $(Ba_{0.85}Sr_{0.15})_{1-x}Pb_xTiO_3$ Ceramic System for $0.02 \leq x \leq 0.08$. *ACS Omega* **2024**, *9* (33), 35548−35559.
(36) Lee, J.; Nam, K.; Ku, B.; Choi, M.; Cho, M.-K.; Jung, S. Y.; Min, J.; Ahn, J.; Lee, Y.; Lee, S.-Y.; Lee, D.; Cho, Y. S.; Kwon, D.-S.; Yoo, J.-K.; Kang, J.; Kim, J. 2D Phosphorene-Decorated Ni-Rich Layered Cathodes for High-Power and High-Energy Li-Ion Batteries. *Adv. Funct. Mater.* **2026**, *36* (9), No. e11385.
(37) Ahn, J.; Kim, T.; Hwang, S.; Son, H. J.; Yun, Y. J.; Ko, Y.; Jun, Y. Strain Relaxed $Cs_\alpha FA_{1-\alpha}PbI_{3-\beta}Cl_\beta$ Perovskite by Intercalation of Cesium via Antisolvent Engineering for Efficient Photovoltaic Devices over 22.9%. *Chem. Eng. J.* **2025**, *520*, 166122.
(38) Singh, A. K.; Yadav, A. N.; Srivastava, A.; Haldar, K. K.; Tomar, M.; Alaferdov, A. V.; Moshkalev, S. A.; Gupta, V.; Singh, K. CdSe/V_2O_5 Core/Shell Quantum Dots Decorated Reduced Graphene Oxide Nanocomposite for High-Performance Electromagnetic Interference Shielding Application. *Nanotechnology* **2019**, *30* (50), 505704.
(39) Stankovich, S.; Dikin, D. A.; Piner, R. D.; Kohlhaas, K. A.; Kleinhammes, A.; Jia, Y.; Wu, Y.; Nguyen, S. T.; Ruoff, R. S. Synthesis of Graphene-Based Nanosheets via Chemical Reduction of Exfoliated Graphite Oxide. *Carbon* **2007**, *45*, 1558−1565.
(40) Wang, Y.-J.; Chu, L.-L.; Tu, Y.-H.; Tsao, L.-H.; Fan, M.-K.; Chen, W.-T.; Chen, C.-W.; Chang, C.-Y.; Chang, Y.-C.; Chueh, Y.-L.; Chiu, P.-W.; Yeh, C.-H.; Chu, Y.-H. Semiconductor Performance Optimization on Quasi-Two-Dimensional $Bi_2O_2(S_xSe_{1-x})$ through Monotonous Alloying. *Nano Lett.* **2025**, *25* (20), 8186−8193.
(41) Bi, H.-X.; Yin, X.-Y.; He, J.-Y.; Song, H.; Lu, S.-J.; Ma, Y.-Y.; Han, Z.-G. Conjugated Organic Component-Functionalized Hourglass-type Phosphomolybdates for Visible-Light Photocatalytic Cr(VI) Reduction in Wide pH Range. *Rare Met.* **2023**, *42*, 3638−3650.
(42) Murphy, M. W.; Yiu, Y. M.; Ward, M. J.; Liu, L.; Hu, Y.; Zapien, J. A.; Liu, Y.; Sham, T. K. Electronic Structure and Optical Properties of CdS_xSe_{1-x} Solid Solution Nanostructures from X-ray Absorption Near Edge Structure, X-ray Excited Optical Luminescence, and Density Functional Theory Investigations. *J. Appl. Phys.* **2014**, *116*, 193709.
(43) Gokbayrak, A. A.; Delikanli, S.; Gorkan, T.; Isik, F.; Durmusoglu, E. G.; Durgun, E.; Demir, H. V. Selenium Alloying in CdSeTe Colloidal Quantum Wells as an Effective Strategy for High Efficiency and Enhanced Stability. *Chem. Mater.* **2026**, *38*, 773−781.
(44) Zakariyya, Y.; Hafeez, H. Y.; Al-Ahmary, K. M.; Al-Mhyawi, S. R.; Alabbad, E. A.; Aboras, A. A.; Mohammed, J.; Suleiman, A. B. Overcoming Photocorrosion in CdS-Based Photocatalyst via MoS_2/rGO Cocatalyst Decoration: A Facile Strategy for Sustainable H_2 Production. *Mater. Chem. Phys.* **2026**, *353*, 132057.
(45) Kar, S.; Pal, T.; Ghosh, S. Reduced Graphene Oxide-SnSe Nanocomposite Photocatalyst with High Apparent Quantum Yield for the Photodegradation of Norfloxacin. *ACS Appl. Nano Mater.* **2024**, *7*, 6516−6524.
(46) Kiani, D.; Wachs, I. E. Practical Considerations for Understanding Surface Reaction Mechanisms Involved in Heterogeneous Catalysis. *ACS Catalysis* **2024**, *14* (22), 16770−16784.
(47) Ghosh, S.; Nandi, S.; De, S.; Pal, T.; Ghosh, S. Solution-Processed $CdS_{1-x}Se_x$ Nanorods with Composition-Tuned Bandgap and Microstructural Evolution for Visible-Light Photocatalytic Response. *J. Phys. Chem. Solids* **2026**, *212*, 113565.
(48) Ghosh, S.; Kar, S.; Pal, T.; Ghosh, S. Sunlight-Driven Photocatalytic Degradation of Norfloxacin Antibiotic in Wastewater by ZnSe Microsphere Functionalized RGO Composite. *Sustainable Chem. Environ.* **2023**, *4*, 100038.
(49) Borthakur, P.; Das, M. R.; Szunerits, S.; Boukherroub, R. CuS Decorated Functionalized Reduced Graphene Oxide: A Dual Responsive Nanozyme for Selective Detection and Photoreduction of Cr(VI) in an Aqueous Medium. *ACS Sustain. Chem. Eng.* **2019**, *7* (19), 16131−16143.
(50) Kar, S.; Ghosh, S.; Pal, T. MoS_2-CdS Composite for Photocatalytic Reduction of Hexavalent Chromium and Thin Film Optoelectronic Device Applications. *Sci. Rep.* **2024**, *14* (1), 18674.
(51) Jalilian, E.; Jafarzadeh, M. Synergistic Enhancement of Photocatalytic Cr(VI) Reduction Using NH_2-UiO-66/Fe-BiOX (X = Cl/I) Nanocomposites under Visible Light. *Langmuir* **2025**, *41*, 22375−22389.
(52) Wang, J.; Lin, C.; Chen, G.; Jiang, J.; Wei, Z.; Li, Y.; Zhou, S.; Yang, F.; Kong, Y. Constructing Carbon-Defect-Rich g-C_3N_4/In_2S_3 2D Vertically Stacked Z-Scheme Heterojunction for Ultrafast Photocatalytic Cr(VI) Reduction. *Appl. Surf. Sci.* **2025**, *687*, 162286.
(53) Kamat, P. V. Graphene-Based Nanoarchitectures. Anchoring Semiconductor and Metal Nanoparticles on a Two-Dimensional Carbon Support. *Phys. Chem. Lett.* **2010**, *1*, 520−527.
(54) Tsai, K.-A.; Hsu, Y.-J. Graphene Quantum Dots Mediated Charge Transfer of CdSe Nanocrystals for Enhancing Photoelectrochemical Hydrogen Production. *Appl. Catal., B* **2015**, *164*, 271−278.

https://doi.org/10.1021/acsanm.6c00578
ACS Appl. Nano Mater. XXXX, XXX, XXX−XXX